

Lévy Walks and Path Chaos in the Dispersal of Elongated Structures Moving across Cellular Flows

Shi-Yuan Hu,^{1,2} Jun-Jun Chu,³ Michael J. Shelley,^{1,4,*} and Jun Zhang^{1,2,5,†}

¹*Applied Mathematics Lab, Courant Institute of Mathematical Sciences,
New York University, New York, NY 10012, USA*

²*Department of Physics, New York University, New York, NY 10003, USA*

³*School of Physics Science and Engineering, Tongji University, Shanghai 200092, China*

⁴*Center for Computational Biology, Flatiron Institute, New York, NY 10010, USA*

⁵*NYU-ECNU Institute of Physics at NYU Shanghai, Shanghai 200062, China*

(Dated: June 19, 2022)

In cellular vortical flows, short but flexible filaments can show simple random walks through their stretch-coil interactions with flow stagnation points. Here, we study the dynamics of semi-rigid filaments long enough to broadly sample the vortical field. Using simulation, we find a surprising variety of long-time transport behavior – random walks, ballistic transport, and trapping – depending upon the filament’s relative length and effective flexibility. Moreover, we find that filaments execute Lévy walks whose diffusion exponents generally decrease with increasing filament length, until transitioning to Brownian walks. Lyapunov exponents likewise increase with length. Even completely rigid filaments, whose dynamics is finite-dimensional, show a surprising variety of transport states and chaos. Fast filament dispersal is related to an underlying geometry of “conveyor belts”. Evidence for these various transport states are found in experiments using arrays of counter-rotating rollers, immersed in a fluid and transporting a flexible ribbon.

Flows at low Reynolds number (Re) are typically laminar and regular. However, chaotic or turbulent dynamics can emerge, such as by flowing through complex geometries [1], adding elastic polymers [2–4], and exploiting the hydrodynamic interactions between suspended passive particles in externally driven flows [5], or between active motile ones [6, 7]. The understanding of how random and complex dynamics can emerge in simple flows at low Re is important in numerous applications [8–15].

Time-independent cellular flows, namely arrays of counter-rotating vortices, are simple flows with inherent characteristic scales and closed streamlines. They often arise as simplified models for flows in nature [16–18] and have been realized in different experiments [19–21]. Tracer particles in such flows simply follow closed streamlines. When the particle size is negligible compared with the characteristic flow scale, complex dynamics, such as aggregation [22] and Lévy walks [18, 23, 24], have been found for active particles. For passive flexible filaments, which can show complex deformations even in simple shear flow [25], complex dynamics arises differently: driven by buckling instabilities near the flow stagnation points, the filaments behave as Brownian walkers across the array [21, 26, 27]. The recent literature on filament dynamics is reviewed in Ref. [28].

For finite-extent filaments, transport is determined by flows sampled nonlocally along the filament, in contrast to small or compact particles. Complex and different behaviors may be generated and controlled through the coupling of flows and filaments at different length scales. In this Letter, we use experiments and a comprehensive set of numerical simulations to investigate the transport of rigid and semi-rigid filaments when their length L is

comparable to the vortex size W in an idealized Stokesian cellular flow. In this regime, the background vortices can be viewed as ‘soft’ scatters for the filaments and the dynamics shows similarity to billiards systems [29–31]. We construct a phase diagram that shows the rich variety of transport states possible for filaments moving across this simple low- Re flow. In particular, we find that as L/W increases, there exists a transition through Lévy walks, of generally decreasing diffusion exponents and increasing Lyapunov exponents, to Brownian walks. Lévy walks have been found in the dynamics of active elongated particles in cellular flows when $L/W \ll 1$, but arising there due to particle motility [18]. Quite remarkably, even completely rigid filaments, described by only center-of-mass (CoM) position and orientation, show these varieties of random walks and chaotic motions.

Besides L and W , the dynamics of a flexible filament depends also upon its elastohydrodynamic length $l_e \sim (B/\mu U_0)^{1/3}$ [32], where B is filament rigidity, μ is fluid viscosity, and U_0 is the characteristic flow velocity. The interplay among the three length scales are captured by two dimensionless control parameters: the relative length $\gamma = L/W$ and the effective flexibility $\eta \propto (L/l_e)^3$. The filament appears to be more ‘flexible’ when η is larger.

Motivating Experiment.—We set up a cellular flow structure by immersing a square 9-by-9 roller array into a tank of pure glycerol (see Fig. 1 and details in supplemental material [33]). The rollers are interconnected and driven by a stepper motor. Through viscous coupling each roller rotates the fluid around it, with nearest neighbor rollers being counter-rotating. Flexible ribbons, made from audio tape, are transported in the cellular flow and stay right beneath the fluid surface, resembling

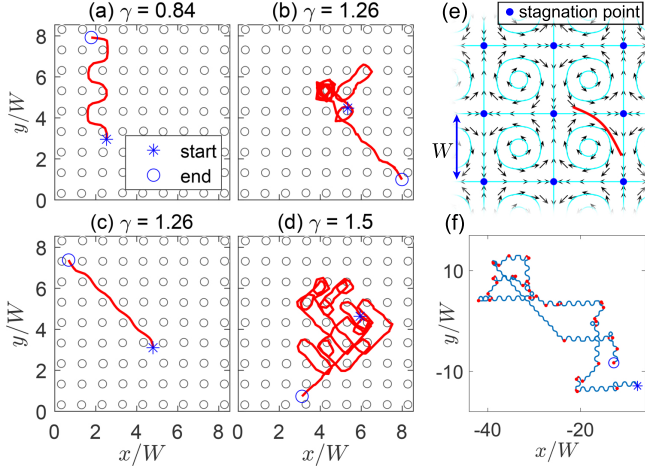


FIG. 1. Experimental CoM trajectories of flexible ribbons in a 9-by-9 cellular flow, as shown on the left. Circles indicate the locations of the spinning rollers. (a) Crenelated step with $\eta \approx 25$. (b) Meandering trajectory with a large diagonal step with $\eta \approx 85$. (c) Diagonal step with $\eta \approx 85$, (d) Meandering trajectory with many turns with $\eta \approx 118$. (e) Snapshot from a numerical simulation with $\eta = 100$ and $\gamma = 1$, showing a flexible filament moving in the cellular flow described by Eq. (1). Black arrows are the background cellular flow and cyan closed curves are the streamlines. (f) A typical trajectory from simulation with $\gamma = 1$ and $\eta = 0.5$. The red points are turning points separating two different steps.

2D motions. The effective flexibility $\eta \approx 7.5\text{--}354$. The $Re = \rho U_0 W / \mu \approx 0.1\text{--}1$, where ρ is the density of glycerol. As shown in Fig. 1, a few interesting patterns of ribbon's motion are identified. For moderate γ , despite occasional trappings, the ribbons can reach the edge of the cellular flow through directional diagonal steps or crenelated steps along $\pm x$ or $\pm y$ directions [Figs. 1(a)–(c)]. However, for larger γ , the ribbons may meander around for a long time and make many turns before getting to the edge [Fig. 1(d)]. When η is sufficiently large, the ribbons are bent with large deformation and often trapped inside one of the fluid vortices.

Simulation and Model.—As a model, we consider flexible and slender filaments of radius R and length L (with aspect ratio $\epsilon = R/L \ll 1$) moving in a Stokesian flow. Lengths are scaled on L , velocity on U_0 , and time on L/U_0 . The stream function Φ_γ of the background flow \mathbf{U} is given by

$$\Phi_\gamma = (\pi\gamma)^{-1} \sin(\pi\gamma x) \sin(\pi\gamma y), \quad (1)$$

which has stagnation points at $(n, m)\gamma^{-1}$ for n, m integers. The unit periodic cell is composed of four counter-rotating vortices [Fig. 1(e)]. The filament centerline, denoted $\mathbf{r}(s, t)$, is parametrized by a signed arclength $s \in [-1/2, 1/2]$. From the leading-order slender body approximation [34], the centerline velocity \mathbf{r}_t is governed by a local balance of drag force with the filament force

upon the fluid,

$$\eta(\mathbf{r}_t - \mathbf{U}[\mathbf{r}]) = (\mathbf{I} + \mathbf{r}_s \mathbf{r}_s) (-\mathbf{r}_{ssss} + (T \mathbf{r}_s)), \quad (2)$$

where the effective flexibility $\eta = 8\pi\mu U_0 L^3 / cB$ with $c = |\log(\epsilon^2 e)|$ and $\mathbf{U}[\mathbf{r}]$ is the background flow evaluated along the filament centerline. The filament force (per unit length) is described by Euler-Bernoulli elasticity: $\mathbf{f} = \mathbf{r}_{ssss} - (T \mathbf{r}_s)_s$, where T is the line tension. Equation (2) is evolved numerically using a second-order finite difference method and implicit time-stepping, while imposing zero-force and -torque boundary conditions.

The case of a rigid straight filament is informative. We take $\mathbf{r}(s, t) = \mathbf{r}_c(t) + s\hat{\mathbf{p}}(t)$, where \mathbf{r}_c is the CoM position and $\hat{\mathbf{p}} = (\cos \theta_c, \sin \theta_c)$ with θ_c the filament orientation. Under zero-force and -torque conditions, the equations of motion are purely kinematic:

$$\dot{\mathbf{r}}_c = -\nabla_{\mathbf{r}_c}^\perp \mathcal{H} \text{ with } \mathcal{H} = \int_{-1/2}^{1/2} \Phi_\gamma[\mathbf{r}(s, t)] ds, \quad (3)$$

$$\dot{\theta}_c = 12\mathcal{H} - 6(\Phi_\gamma[\mathbf{r}(1/2, t)] + \Phi_\gamma[\mathbf{r}(-1/2, t)]), \quad (4)$$

where $\nabla^\perp = (-\partial_y, \partial_x)$. In the “point limit” $\gamma = 0$, particle transport [Eq. (3)] is Hamiltonian, local, and decoupled from particle rotational dynamics. Increasing γ increases the averaging (over particle length) of the background flow, while also increasing the coupling of particle translation to rotation. This increase in system dimension leads to loss of integrability and allows for transport chaos. Equations (3) and (4) are evolved using a fourth-order Runge-Kutta scheme. Our simulations typically run for $2 \times 10^4 L/U_0$ to capture long-time dynamics.

Simulation results.—The filament CoM trajectories show strong dependence on γ and the initial conditions. A common statistical measure of a complex trajectory is

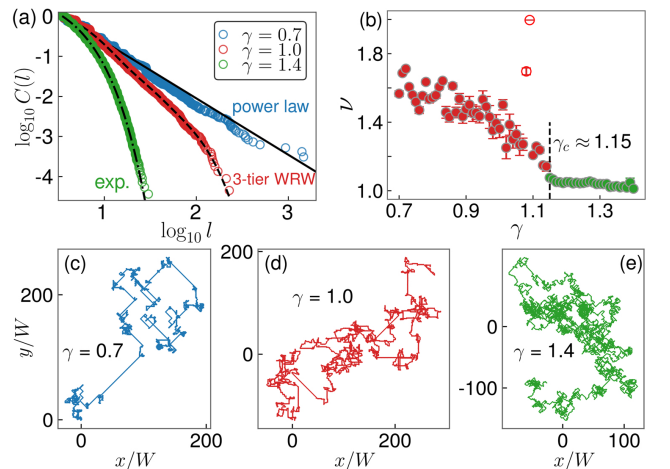


FIG. 2. From Lévy walks to Brownian walks for rigid filaments. (a) $C(l)$ for $\gamma = 0.7, 1.0$, and 1.4 , with best-fit distributions. (b) Scaling exponent ν as a function of γ . Error bars represent uncertainties due to initial conditions. Open circles: $\gamma = 1.08$ and $\gamma = 1.09$. (c)–(e) Typical trajectories corresponding to the three cases shown in (a).

its step-length distribution $\phi(l)$ [35]. We define a step to be a diagonal step or a crenelated step. The step-length l is the straight-line distance between successive turning points, which separate two steps along different directions (see Fig. 1(f) and Ref. [33]). For rigid filaments of different γ , Fig. 2(a) shows the complement of the cumulative distribution, $C(l) = 1 - \int_a^l \phi(l)dl$, for l in 100 trajectories with random initial conditions. We fit several random walk models using a maximum likelihood method [36, 37]. When $\gamma = 0.7$, the best-fit model is a power law given by $\phi(l) \propto l^{-(1+\beta)}$ with $\beta \approx 1.4$, indicating Lévy walks [35]. Clusters of short steps are interspersed with long steps between them [Fig. 2(c)]. When γ is increased to 1.4, the best-fit model is an exponential distribution and the filaments display Brownian walks with clusters of small steps within the trajectories [Fig. 2(e)]. At an intermediate value of γ , the best-fit model is a Weierstrassian random walk (WRW), which has been found in the studies of animal search strategies and random walks in bacteria swarms [18, 38–40]. The $\phi(l)$ of the WRW is given by a hierarchical sum of exponential distributions with mean $b^{-(j+1)}$ weighted by $q^{-(j+1)}$: $\phi(l) \propto \sum_{j=0}^J q^{-(j+1)} b^{j+1} \exp(-b^{j+1}l)$, which resembles a power law when $J \rightarrow \infty$ and degenerates into an exponential distribution when $J = 0$.

The above transition through Lévy walks to Brownian walks can be confirmed from the MSD scaling exponent [41], $\langle \delta^2(\tau) \rangle \sim \tau^\nu$ [Fig. 2(b)]. For Lévy walks the scaling exponent $\nu = 3 - \beta$ if $1 < \beta < 2$ [35], and for Brownian walks $\nu = 1$. In general, ν decreases as γ increases. The critical γ separating the two transport behaviors is around 1.15. Two exceptionally large values of ν exist at $\gamma = 1.08$ and 1.09, which are due to a perfect match of the filament length to the periodic flow geometry and unstable under small perturbations of the flow field [33]. As shown in Fig. 3(a), the transition is accompanied with a growth in the Lyapunov exponent λ [42, 43]: Brownian walks are more chaotic than Lévy walks. A transition from Lévy walks to Brownian walks has been found in the transport of ions in optical lattice [44, 45]. The presence of Lévy walks is also known in Hamiltonian chaos, but the transitions are typically abrupt [46–49].

Mechanism.—We attribute the emergence of chaos and different random walks to the nonlocal geometrical averaging of the background flow by the filament from its broad extension across vortices. Consider rigid filament, from Eq. (3), the CoM velocity of the filament is $\mathbf{v}_c = (u_c, v_c) = \int_{-1/2}^{1/2} \mathbf{U}[\mathbf{r}(s)]ds$. We first compute the variance of $\mathbf{U}[\mathbf{r}(s)]$: $\text{Var}(\mathbf{U}[\mathbf{r}]) = \langle \int_{-1/2}^{1/2} (\mathbf{U}[\mathbf{r}(s)] - \mathbf{v}_c)^2 ds \rangle$, where the average is taken with respect to \mathbf{r}_c over the entire unit cell and θ_c over $[0, 2\pi)$. With the increase of γ [Fig. 3(b) left], $\text{Var}(\mathbf{U}[\mathbf{r}])$ becomes larger, i.e., the background flow that the filament experienced on average becomes more variable. We also compute the correlation

function between the unit velocity vectors of filament's two ends ($s = 1/2, -1/2$): $C_v = \langle \hat{\mathbf{v}}(-1/2) \cdot \hat{\mathbf{v}}(1/2) \rangle$, where the average is along CoM trajectories [Fig. 3(b) right]. When C_v is large, the filament is likely to be translated along a flow but to be turned around when C_v is small. Both $\text{Var}(\mathbf{U}[\mathbf{r}])$ (increasing with γ) and C_v (decreasing with γ) show that long filaments with large γ can hardly travel long unidirectional steps but rather turn around and take seemingly random and diffusive motions. On the other extreme at very small γ , filaments are too short to perceive any flows outside the local circulation it resides and most of the filaments are trapped except those initially close to the separatrices. Therefore, the only possible long-distance travelers are those filaments of intermediate lengths.

Indeed, we find some clues by mapping the spatial distributions of x -component CoM velocity $u_c(\mathbf{r}_c, \theta_c)$. In Figs. 3(c)–3(e), the maps of u_c were made with $\theta_c = 3\pi/4$, but any other values of θ_c in the second and fourth quadrants would result in similar maps but slightly smaller magnitude of u_c . When $\gamma \ll 1$ [Fig. 3(c)], areas of positive u_c values (red, rightward motion) and negative u_c values (blue, leftward motion) are isolated from each other, filament cannot travel across vortices. As γ increases, the red and blue regions start to deform and morph into many alternating ‘conveyor belts’ flowing towards opposite directions [Figs. 3(d), 3(e)]. If θ_c lies in the first and third quadrants, the ‘conveyor belts’ will take the other diagonals oriented $\pi/2$ from those in Figs. 3(d) and 3(e). The filament can now move across vortices and travel long steps. We see two competing effects at work as γ further increases: longer filament promotes the formation of ‘conveyor belts’ but at the

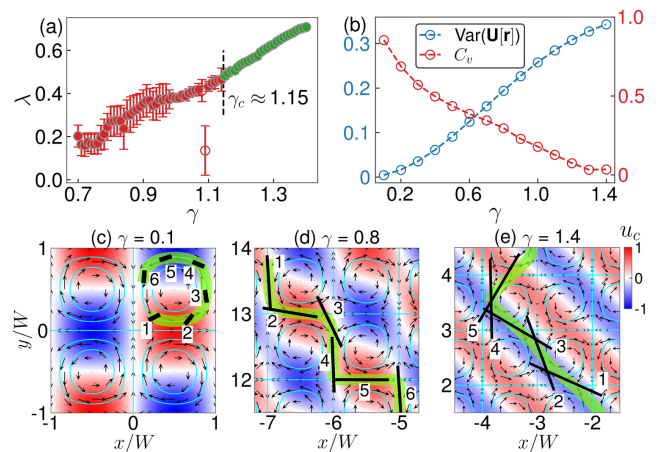


FIG. 3. (a) Lyapunov exponent λ as functions of γ for rigid filament. The large error bars for Lévy walks are due to the nonuniformity of the phase space. (b) $\text{Var}(\mathbf{U}[\mathbf{r}])$ (left) and C_v (right) as a function of γ . (c), (d), and (e) Maps of positive u_c (red, rightward motion) and negative u_c (blue, leftward motion) computed with $\theta_c = 3\pi/4$ (see text for detail). Snapshots of the motion of rigid filaments are also shown with the time ordering labeled by numbers. Green thick lines trace the CoM trajectories.

same time it is more likely to turn and change directions. The latter effect is demonstrated in Fig. 3(e) as a long filament is captured first by an opposite ‘conveyor belt’ (label 4) and then turns (label 5) with its two ends moving oppositely.

The patterns of filament dispersal at scales much larger than W are significantly different for different random walks. For those performing Lévy walks they are strikingly anisotropic. Figure 4(a) shows that for $\gamma = 0.7$, the probability density function (PDF) $P(\mathbf{x}, t)$ of finding a filament at position \mathbf{x} at time t after starting off with random initial conditions from the unit cell centered at the origin has a ‘ \star ’-like structure with four branches extending along the diagonals specified by (\hat{d}_1, \hat{d}_2) . Such anisotropy arises from the long unidirectional diagonal steps due to the ‘conveyor belts’. In particular, a sharp peak exists at the far front of each branch [Fig. 4(b)] reflecting the microscopic geometry of the Lévy walks [50]: filaments can only move along \hat{d}_1 or \hat{d}_2 at each step. The PDF along \hat{d}_1 is given by a product of a 1D Lévy distribution and a pre-factor that accounts for the decrease in the spread of the PDF along \hat{d}_2 [50],

$$P(d_1, t) \propto (1 - d_1/(ct))^{-1/\beta} \mathcal{L}_\beta^\sigma(d_1), \quad (5)$$

where c is the average speed of the filaments and \mathcal{L}_β^σ is a 1D Lévy distribution with exponent β and scale parameter σ ($\propto t^{1/\beta}$). Equation (5) agrees well with the simulation result [Fig. 4(d)]. As γ increases, crenelated steps along $\pm x$ or $\pm y$ directions become more frequent and 8-fold ‘ \star ’-like patterns are formed [Fig. 4(b)]. While almost unapparent, these additional branches can be faintly discerned in Fig. 4(a). Eventually in the Brownian-walk regime for sufficient large γ , in sharp contrast to Lévy walks, the PDF follows an isotropic 2D Gaussian distribution with its variance scaling linearly with time t [Fig. 4(c)].

By extensively surveying the phase space of γ and η , for

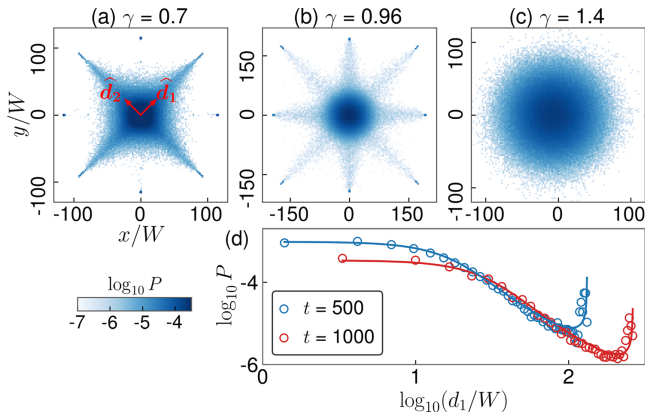


FIG. 4. Dispersal patterns of 10^6 rigid filaments. Probability density function (PDF) $P(x, y)$ at $t = 500$ for (a) $\gamma = 0.7$, (b) $\gamma = 0.96$, and (c) $\gamma = 1.4$. (d) PDF along direction \hat{d}_1 shown in (a) at two different time instants for $\gamma = 0.7$. Solid lines are the fittings of the theoretical result given by Eq. (5).

the first time, we construct a phase diagram showing various transport states (see Fig. 5(a) and Ref. [33]). Highly flexible filaments ($\eta \gtrsim 10^2$) are deformed and trapped inside vortices for all values of γ , as is also observed in the experiments. For relatively rigid filaments ($\eta \lesssim 10$), the transport states are determined by γ . The boundary that separates Lévy walks ($1 < \nu < 2$) and Brownian walks ($\nu \approx 1$) is located around $\gamma = 1.15$. At intermediate η between $10 - 10^2$, the filament first meanders around for a short period before moving unidirectionally and indefinitely along diagonal steps or crenelated steps. We call this type of transport behavior a ballistic state with $\nu \approx 2$. Even within the ballistic state, the filament dispersal patterns show strong dependence on both γ and η and filaments with different lengths and flexibility are dynamically sorted [33]. The dispersal rate of filaments is largest in ballistic state, followed by Lévy walks and then Brownian walks. There is no long-range transport in the trapping state.

Experimental evidence.—We find evidence that shorter ribbons perform Lévy walks while longer ribbons perform Brownian walks in the experiments [33]. Figures 5(b) and 5(c) show two examples. For $\gamma = 1.26$, the best-fit model is truncated power law (TPL) [51] supporting a Lévy walk; for $\gamma = 1.5$, the step length distribution $C(l)$ better resembles a truncated exponential (TE) model supporting a Brownian walk. The γ value that separates the two states is estimated to be around 1.4, which differs from the value found in the simulation. This discrepancy is possibly caused by the presence of the roller boundaries. Despite the subtle difference in $C(l)$ due to the limited size of the flow field in the experiments, the trajectories for the two states are significantly different from each other as depicted in Fig. 1: with more turns in the trajectories, longer ribbons take much longer time to reach the edge of the flow field than shorter ribbons. Our experiments on the effect of η are limited, but for large η ,

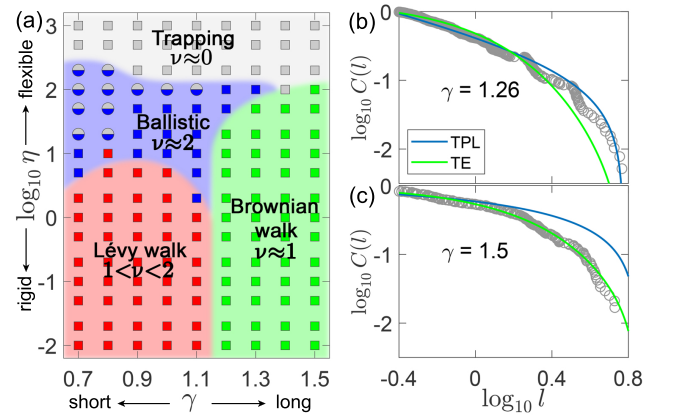


FIG. 5. (a) From simulation, the phase diagram of the transport states. WRWs are classified as Lévy walks. Ballistic state coexisting with trapping state are marked by circles. (b), (c) $C(l)$ from 52 trajectories in experiments for two different values of γ .

the ribbon is typically bent around one of the rollers and trapped for long time.

Discussion.—Our experiments and simulations demonstrate that this simple system of a semi-rigid filaments moving in a Stokesian cellular vortical flows has a surprisingly rich range of dispersal dynamics, including Lévy walks and path chaos. For $\gamma \gg 1$ our limited simulations show mostly Brownian walks due to averaging over multiple vortices. The emergence of cross-vortex motion and chaos in our system does not require the flow itself to be time-dependent and chaotic as it does for tracer particles [17, 52]. It arises from the elongated body being able to broadly sample the background vortical field, and the strong coupling of rotational to translational dynamics afforded by that elongation. The cross-streamline motion and escape from local flows shown by the semi-rigid filaments have implications for efficient fluid mixing at low Re by additives [8, 53]. Similar to the billiards system [29, 30], the anisotropic dispersals of filaments in the Lévy-walk state and ballistic state are also originated from long unidirectional steps pre-programmed by the fundamental geometries of the backgrounds. However, the dominant directions of motion depend on the relative length γ and effective flexibility η of filaments in our system but are fully specified by the geometries of scatterers in the billiards. Most prominently, various transport states can be achieved by tuning different length scales, which also serves as the underlying mechanism of gel electrophoresis [55]. Our results may open up new possibilities for efficient dynamical sorting of elongated particles and semi-flexible biopolymers [54–57].

We thank L. Ristroph, E.A. Spiegel, Y.-N. Young, and J.-Q. Zhong for inspiring questions and helpful discussions. S.Y.H. gratefully acknowledge the MacCracken Fellowship provided by New York University. M.J.S. and J.Z. acknowledge support from National Science Grant CBET-1805506, and J.Z. acknowledges support from NSFC-11472106.

* shelley@cims.nyu.edu

† jun@cims.nyu.edu

- [1] A. D. Stroock, S. K. W. Dertinger, A. Ajdari, I. Mezić, H. A. Stone, and G. M. Whitesides, *Science* **295**, 647–651 (2002).
- [2] A. Groisman and V. Steinberg, *Nature* **405**, 53–55 (2000).
- [3] P. E. Arratia, C. C. Thomas, J. Diorio, and J. P. Gollub, *Phys. Rev. Lett.* **96**, 144502 (2006).
- [4] V. Steinberg, *Annu. Rev. Fluid Mech.* **53**, 27–58 (2021).
- [5] D. J. Pine, J. P. Gollub, J. F. Brady, and A. M. Leshansky, *Nature* **438**, 997–1000 (2005).
- [6] C. Dombrowski, L. Cisneros, S. Chatkaew, R. E. Goldstein, and J. O. Kessler, *Phys. Rev. Lett.* **93**, 098103 (2004).
- [7] D. Saintillan and M. J. Shelley, *C. R. Phys.* **14**, 497–517 (2013).
- [8] A. Groisman and V. Steinberg, *Nature* **410**, 905–908 (2001).
- [9] H. A. Stone, A.D. Stroock, and A. Ajdari, *Annu. Rev. Fluid Mech.* **36**, 381–411 (2004).
- [10] C.-Y. Lee, C.-L. Chang, Y.-N. Wang, and L.-M. Fu, *Int. J. Mol. Sci.* **12**, 3263–3287 (2012).
- [11] K. Ward and Z. H. Fan, *J. Micromech. Microeng.* **25**, 094001 (2015).
- [12] J. Nam, H. Lim, D. Kim, H. Jung, and S. Shin, *Lab Chip* **12**, 1347–1354 (2012).
- [13] S. Yazdi and A. M. Ardekani, *Biomicrofluidics* **6**, 044114 (2012).
- [14] A. Karimi, S. Yazdi, and A. M. Ardekani, *Biomicrofluidics* **7**, 021501 (2013).
- [15] X. Lu, C. Liu, G. Hu, and X. Xuan, *J. Colloid Interface Sci.* **500**, 182–201 (2017).
- [16] H. Stommel, *J. Mar. Res.* **8**, 24 (1949).
- [17] T. H. Solomon and J. P. Gollub, *Phys. Rev. A* **38**, 6280 (1988).
- [18] G. Ariel, A. Be’er, and A. Reynolds, *Phys. Rev. Lett.* **118**, 228102 (2017).
- [19] D. Rothstein, E. Henry, and J. P. Gollub, *Nature* **401**, 770–772 (1999).
- [20] N. T. Ouellette and J. P. Gollub, *Phys. Rev. Lett.* **99**, 194502 (2007).
- [21] E. Wandersman, N. Quennou, M. Fermigier, A. Lindner, and O. du Roure, *Soft matter* **6**, 5715–5719 (2010).
- [22] C. Torney and Z. Neufeld, *Phys. Rev. Lett.* **99**, 078101 (2007).
- [23] G. Ariel, A. Rabani, S. Benisty, J. D. Partridge, R. M. Harshey, and A. Be’er, *Nat. Commun.* **8**, 8396 (2015).
- [24] G. Ariel and J. Schiff, *Physica D* **411**, 132584 (2020).
- [25] J. LaGrone, R. Cortez, W. Yan, and L. Fauci, *J. Non-newton Fluid Mech.* **269**, 73–81 (2019).
- [26] Y.-N. Young and M. J. Shelley, *Phys. Rev. Lett.* **99**, 058303 (2007).
- [27] N. Quennou, M. Shelley, O. du Roure, and A. Lindner, *J. Fluid Mech.* **769**, 387–402 (2015).
- [28] O. du Roure, A. Lindner, E. Nazockdast, and M. J. Shelley, *Annu. Rev. Fluid Mech.* **51**, 539–572 (2019).
- [29] L. Zarfaty, A. Peletskyi, I. Fouxon, S. Denisov, and E. Barkai, *Phys. Rev. E* **98**, 010101(R) (2018).
- [30] L. Zarfaty, A. Peletskyi, E. Barkai, and S. Denisov, *Phys. Rev. E* **100**, 042140 (2019).
- [31] R. Klages, Sol Selene Gil Gallegos, J. Solanpää, M. Sarvilahti, and E. Räsänen, *Phys. Rev. Lett.* **122**, 064102 (2019).
- [32] C. H. Wiggins and R. E. Goldstein, *Phys. Rev. Lett.* **80**, 3879 (1998).
- [33] See Supplemental Material for videos showing the motion of filaments in different states, experimental details, step length analysis, and dispersal patterns in ballistic state.
- [34] J. B. Keller and S. I. Rubinow, *J. Fluid Mech.*, **75**, 705–714 (1976).
- [35] V. Zaburdaev, S. Denisov, and J. Klafter, *Rev. Mod. Phys.* **87**, 483 (2015).
- [36] A. Edwards *et al.*, *Nature* **449**, 1044–1048 (2007).
- [37] A. Clauset, C. R. Shalizi, and M. E. J. Newman, *SIAM Rev.* **51**, 661–703 (2009).
- [38] B. D. Hughes, M. F. Shlesinger, and E. W. Montroll, *Proc. Natl. Acad. Sci. U.S.A.* **78**, 3287–3291 (1981).
- [39] A. M. Reynolds, P. Schultheiss, and K. Cheng, *J. Theor.*

- Biol. **340**, 17-22 (2014).
- [40] A. M. Reynolds, Sci. Rep. **4**, 4409 (2014).
 - [41] R. Metzler, J.-H. Jeon, A. G. Cherstvy, and E. Barkai, Phys. Chem. Chem. Phys. **16**, 24128 (2014).
 - [42] G. Benettin, L. Galgani, A. Giorgilli, and J.M. Strelcyn, Meccanica **15**, 21–30 (1980).
 - [43] K. Ramasubramanian and M.S. Sriram, Physica D **139**, 72–86 (2000).
 - [44] S. Marksteiner, K. Ellinger, and P. Zoller, Phys. Rev. A. **53**, 3409 (1996).
 - [45] H. Katori, S. Schlipf, and H. Walther, Phys. Rev. Lett. **79**, 2221 (1997).
 - [46] A. A. Chernikov, B. A. Petrovichev, A. V. Rogal'sky, R. Z. Sagdeev, and G. M. Zaslavsky, Phys. Lett. A **144**, 127-133 (1990).
 - [47] G. M. Zaslavsky, D. Stevens, and H. Weitzner, Phys. Rev. E **48**, 1683 (1993).
 - [48] S. Benkadda, S. Kassibrakis, R. B. White, and G. M. Zaslavsky, Phys. Rev. E **55**, 4909 (1997).
 - [49] M. Harsoula and G. Contopoulos, Phys. Rev. E **97**, 022215 (2018).
 - [50] V. Zaburdaev, I. Fouxon, S. Denisov, and E. Barkai, Phys. Rev. Lett. **117**, 270601 (2016).
 - [51] D. A. Raichlen, B. M. Wood, A. D. Gordon, A. Z. P. Mabulla, F. W. Marlowe, and H. Pontzer, Proc. Natl. Acad. Sci. U.S.A. **111**, 728-733 (2014).
 - [52] T. H. Solomon, E. R. Weeks, and H. L. Swinney, Phys. Rev. Lett. **71**, 3975 (1993).
 - [53] S. H. Lee, D. van Noort, J. Y. Lee, B.-T. Zhang, and T. H. Park, Lab Chip **9**, 479-482 (2009).
 - [54] L. R. Huang, J. O. Tegenfeldt, J. J. Kraeft, J. C. Sturm, R. H. Austin, and E. C. Cox, Nat. Biotechnol. **20**, 1048–1051 (2002).
 - [55] K. D. Dorfman, S. B. King, D. W. Olson, J. D. P. Thomas, and D. R. Tree, Chem. Rev. **113**, 2584-2667 (2013).
 - [56] P. Sajeesh and A. K. Sen, Microfluid Nanofluid **17**, 1–52 (2014).
 - [57] B. Chakrabarti, C. Gaillard, and D. Saintillan, Soft Matter **16**, 5534-5544 (2020).

Supplemental Material for Lévy Walks and Path Chaos in the Dispersal of Elongated Structures Moving across Cellular Flows

Shiyuan Hu,^{1,2} Junjun Chu,³ Michael Shelley,^{1,4,*} and Jun Zhang^{1,2,5,†}

¹*Applied Mathematics Lab, Courant Institute of Mathematical Sciences,
New York University, New York, NY 10012, USA*

²*Department of Physics, New York University, New York, NY 10003, USA*

³*School of Physics Science and Engineering, Tongji University, Shanghai 200092, China*

⁴*Center for Computational Biology, Flatiron Institute, New York, NY 10010, USA*

⁵*New York University-East China Normal University Institute of Physics,
New York University Shanghai, Shanghai 200062, China*

(Dated: June 19, 2022)

VIDEO INFORMATION

Video1 (simulation): Filament in trapping state with $\gamma = 1.2$ and $\eta = 1000$.

Video2 (simulation): Filament in Ballistic state taking crenelated step with $\gamma = 1$ and $\eta = 50$.

Video3 (simulation): Filament in Ballistic state taking diagonal step with $\gamma = 1.2$ and $\eta = 50$.

Video4 (simulation): Filament in Lévy-walk state with $\gamma = 0.9$ and $\eta = 0.1$.

Video5 (simulation): Filament in Brownian-walk state with $\gamma = 1.4$ and $\eta = 0.5$.

Video6 (experiment): Directional motion of ribbon with $\gamma = 1.26$ and $\eta \approx 85$. (Trajectory Duration 30.5 sec.)

Video7 (experiment): Meandering motion of ribbon with $\gamma = 1.5$ and $\eta \approx 118$. (Trajectory Duration 204 sec.)

Occasionally, the experimental center-of-mass (CoM) trajectory lacks smoothness. This is largely due to the imperfect tracking caused by the extremely thin ribbon. When our tracking algorithm processes the video recordings (with a broad view field), it fails at times to recognize the entire filament.

EXPERIMENTAL DETAILS

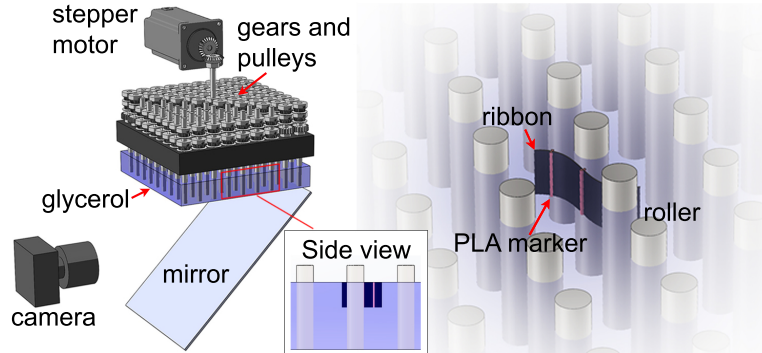


FIG. 1. Schematic of the experimental setup as shown on the left. Right panel details a ribbon moving between rollers.

The experiment setup is shown in Fig. 1. We immerse a square 9-by-9 roller array into a tank of pure glycerol from the above. The fluid surface is free and its bottom is no-slip. The center-to-center distance between the nearest neighbor rollers is $W = 19$ mm, and the diameter of the roller is 6.35 mm. Other parameters are listed in Table I. The rollers are inter-connected with gears, pulleys, and timing belts and driven by a stepper motor, such that nearest neighbor rollers are counter-rotating and rollers in the same diagonal are co-rotating. Each roller rotates the fluid around it through viscous coupling and a cellular flow structure is formed. Different from our method, another way to form cellular flows is using electromagnetic forcing [1].

In our experiments, we transport flexible ribbons made from audio tapes that are slightly denser than glycerol. To prevent the ribbon from sinking, we attach equally-spaced PLA markers, thin rods of 1 mm diameter, to the ribbon

because PLA is lighter than glycerol. As a result, the ribbon stays right beneath the free surface and remains vertical due to the quasi-2D flow. Since the ribbon width is small compared with the depth of the fluid, we can neglect the effect of the no-slip bottom of the tank on ribbon's motion. Therefore, the motion of the ribbon is essentially 2D. The PLA markers can also make the video tracking easier. The motion of the ribbon is recorded by a camera through a reflection mirror at 45° with respect to the horizontal plane. We then process the video using Matlab Image Processing Toolbox and obtain the CoM trajectories.

In the experiment, the two control parameters are the rotation frequency f_0 of the stepper motor and the ribbon length L . We vary f_0 mostly between 0.3 Hz and 1.5 Hz and experiment on three values of L : 16 mm, 24 mm, and 28.5 mm. The effective flexibility η can be estimated. For example, when $L = 24$ mm and $f_0 = 1$ Hz,

$$\eta = \frac{8\pi\mu U_0 L^3}{cB} = \frac{8\pi\mu f_0 L^4}{cB} \approx 121, \quad (1)$$

where μ is the dynamical viscosity of glycerol and the characteristic flow velocity $U_0 = f_0 L$.

Geometric parameters	
distance of neighbor rollers W	19 mm
roller diameters	6.35 mm
fluid depth	25 mm
tank size	171 mm×171 mm×30 mm
Material parameters	
ribbon width	6×10^{-3} m
ribbon thickness	2.54×10^{-5} m
ribbon bending rigidity B	7.6×10^{-9} J·m
ribbon density	$1.3\text{--}1.4 \times 10^3$ kg/m ³
glycerol density	1.26×10^3 kg/m ³
glycerol dynamic viscosity, μ	1.412 Pa·s
PLA density	1.24×10^3 kg/m ³
diameter of PLA marker	1×10^{-3} m

TABLE I. Parameters of the experimental setup.

	η	Distribution	Akaike weights w
$\gamma = 0.82$	25	truncated exponential	0.05
		truncated power law	0.95
$\gamma = 1.26$	35	truncated exponential	0
		truncated power law	1
	85	truncated exponential	0
		truncated power law	1
$\gamma = 1.50$	112	truncated exponential	0.04
		truncated power law	0.96
	118	truncated exponential	1
		truncated power	0
$\gamma = 1.50$	166	truncated power law	1
		truncated power law	0

TABLE II. From experiments, Akaike weights of best-fit truncated power law and truncated exponential distribution for $\gamma = 0.82$, 1.26, and 1.5 with different values of η .

STEP-LENGTH DISTRIBUTION ANALYSIS

The step length l is the straight-line distance between successive turning points separating the diagonal steps and crenelated steps. To identify the turning points, we first find the local minimums and maximums of the x coordinate of the CoM trajectories [Fig. 2], and then calculate the straight-line distances between each two neighbor extremums. If a distance is smaller than a minimum value l_{\min} , we discard the corresponding leading extremum used in computing that distance. The same procedure is repeated for y coordinates. The turning points are the aggregate of the remaining

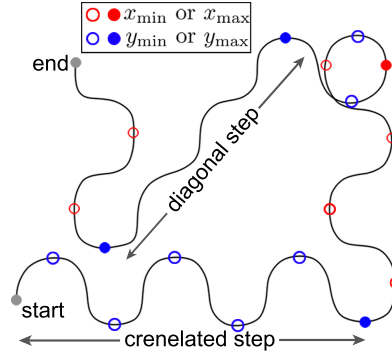


FIG. 2. Determination of the turning points by finding the local minimums and maximums of the x and y coordinates of the CoM trajectory. The red circles are the extremums of x coordinates and the blue circles are the extremums of y coordinates. Open circles are discarded and filled circles are determined turning points (including the start and end points).

extremums of x and y coordinates while keeping their time ordering. We take l_{\min} to be slightly larger than the vortex size W .

After we obtain the step-length data, we fit it to the candidate distributions mentioned in the main text using a maximum likelihood method [2–4]. The Akaike weight w is then calculated for model selection [5]. The data completely supports the distribution when $w = 1$ and does not support the distribution when $w = 0$. The above approach is robust for identifying Lévy-walk patterns.

In the experiments, since the flow field is bounded, we fit the step-length data to the truncated power law and truncated exponential distribution. The Akaike weights for $\gamma = 0.82, 1.26$ and 1.5 with different values of η are shown in Table II. The step-length data for short filaments ($\gamma = 0.82$ and 1.26) better supports truncated power law. For longer filament ($\gamma = 1.5$), the step-length data better supports truncated exponential distribution.

DYNAMICAL SORTING IN THE BALLISTIC STATE

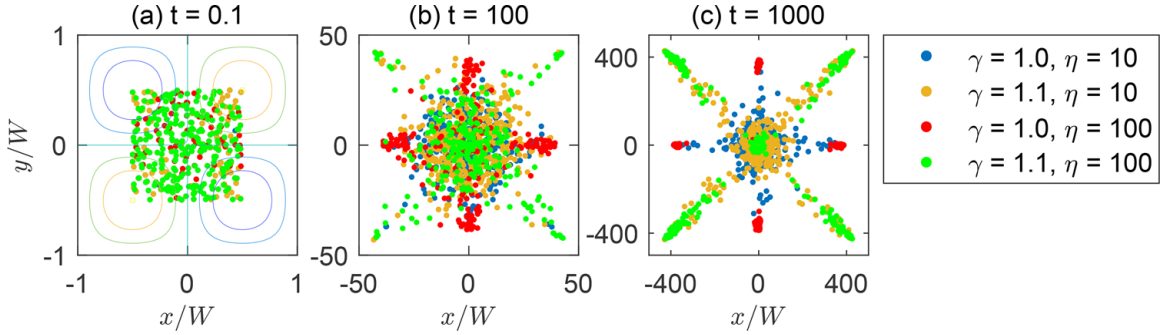


FIG. 3. From simulation, anisotropic dispersals in ballistic state showing the distribution of the CoM positions for four different filament lengths and flexibility: $\gamma = 1, \eta = 10$ (blue), $\gamma = 1.1, \eta = 10$ (yellow), $\gamma = 1, \eta = 100$ (red), and $\gamma = 1.1, \eta = 100$ (green), at (a) $t = 0.1$, (b) $t = 100$, and (c) $t = 1000$.

In the ballistic state, the filament typically meanders around for a short period t_m before taking unidirectional crenelated steps along $\pm x$ and $\pm y$ directions or unidirectional diagonal steps along diagonals. Longer filaments ($\gamma > 1$) are transported along diagonals and shorter filaments ($\gamma \leq 1$) are transported along $\pm x$ and $\pm y$ directions. The dispersals of filaments is anisotropic and depend strongly on γ and η [Fig. 3]. Initially [Fig. 3(a)], four different filaments with different values of γ and η are distributed inside a square region ($x \in [-W/2, W/2]$, $y \in [-W/2, W/2]$) with random initial positions and orientations. The anisotropy in the dispersal patterns grows quickly. When $t = 100$ [Fig. 3(b)], some of the green ($\gamma = 1.1, \eta = 100$) and red filaments ($\gamma = 1, \eta = 100$) are already separated spatially with the green filaments moving along diagonals and red filaments moving along $\pm x$ and $\pm y$ directions. When t is sufficiently large [Fig. 3(c)], four kinds of filaments are already well separated from each other. Filaments with larger η mainly occupy the dispersal fronts, and filaments with smaller η are distributed along diagonals or x and

y directions, i.e., the meandering time t_m decreases as η increases. However, filaments with sufficiently large η will result in trapping state, in which filaments are bent with large deformation and trapped inside one of the vortices.

PERTURBATION OF THE BACKGROUND FLOW

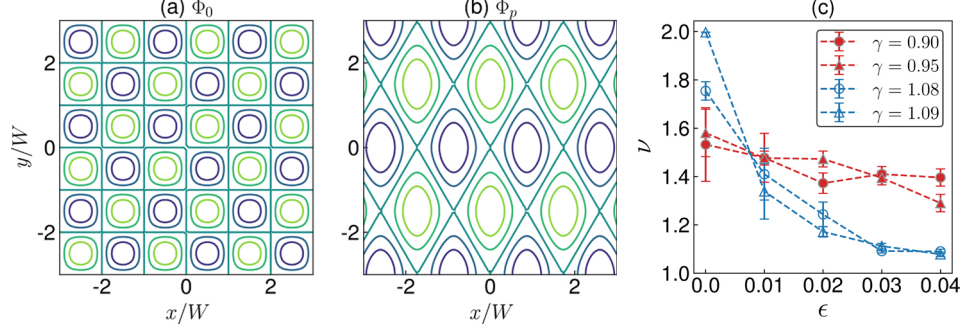


FIG. 4. (a) Unperturbed stream function. (b) Perturbation stream function Φ_p given by Eq. (2) with $\xi = 2/3$, $\alpha = 1/2$ and $\beta = \sqrt{3}/2$. (c) The scaling exponent ν of the mean square displacement as function of ϵ for different values of γ .

In Fig. 2(b) of the main text, there are two exceptionally large values of ν at $\gamma = 1.08$ and $\gamma = 1.09$, representing nearly ballistic motion. This is due to a perfect match of the filament length to the periodic flow geometry, which can be verified by perturbing the background flow. The unperturbed stream function $\Phi_0 = (\pi\gamma)^{-1} \sin(\pi\gamma x) \sin(\pi\gamma y)$. The perturbation stream function Φ_p is given by [6].

$$\Phi_p = (\pi\gamma)^{-1} \sin[\pi\gamma\xi(\alpha x + \beta y)] \sin[\pi\gamma\xi(\alpha x - \beta y)], \quad (2)$$

where ξ controls the characteristic scale of the flow, α and β change the direction of the separatrices [Fig. 4 (b)]. The resulting flow field is given by $\Phi = \Phi_0 + \epsilon\Phi_p$, where ϵ is the perturbation magnitude. We take $\xi = 2/3$, $\alpha = 1/2$ and $\beta = \sqrt{3}/2$, and Φ_p is still spatially periodic but the period is different from that of Φ_0 . Figure 4(c) shows that for $\gamma = 1.08$ and $\gamma = 1.09$, the scaling exponent of the mean square displacement, ν , decreases rapidly as ϵ increases. However, for $\gamma = 0.9$ and 0.95 , ν is relatively stable and decreases much slower.

* shelley@cims.nyu.edu

† jun@cims.nyu.edu

- [1] E. Wandersman, N. Quennouz, M. Fermigier, A. Lindner, and O. du Roure, *Soft matter* **6**, 5715-5719 (2010).
- [2] D. A. Raichlen *et al.*, *Proc. Natl. Acad. Sci. U.S.A.* **111**, 728-733 (2014).
- [3] A. Clauset, C. R. Shalizi, and M. Newman, *SIAM Rev.* **51**, 661-703 (2009).
- [4] A. Edwards *et al.*, *Nature* **449**, 1044-1048 (2007).
- [5] K. P. Burnham and D. R. Anderson., *Model selection and multimodel inference: A practical information-theoretic approach*, Springer-Verlag, New York, USA, (2002).
- [6] G. Ariel, A. Be'er, and A. Reynolds, *Phys. Rev. Lett.* **118**, 228102 (2017).